



# **Cryo-seismicity triggered by ice mass discharge through the Antarctic subglacial hydrographic network**

Stefania Danesi<sup>1</sup>, Simone Salimbeni<sup>1</sup>, Alessandra Borghi<sup>1</sup>, Stefano Urbini<sup>2</sup> and Massimo Frezzotti<sup>3</sup>

<sup>1</sup>Istituto Nazionale di Geofisica e Vulcanologia, Sezione di Bologna, Bologna, Italy

<sup>2</sup>Istituto Nazionale di Geofisica e Vulcanologia, Sezione di Roma2, Roma, Italy

<sup>3</sup>Department of Science, Roma Tre University, Rome, Italy

*Correspondence to:* Stefania Danesi (stefania.danesi@ingv.it)

**Abstract.** We analyse seismic time series collected during experimental campaigns in the area of the David Glacier, South Victoria Land, Antarctica, between 2003 and 2016. We observe hundreds of repeating seismic events, characterised by highly correlated waveforms (cross-correlation  $> 0.95$ ), which mainly occur in the floating area between the grounding and the floating line of the ice stream. The joint analysis of seismic occurrences and observed local tide measurements seems to show that seismicity is not triggered by a seasonal, regular, periodic forcing such as the ocean tide, but more likely by transient irregular impulses. We consider possible environmental processes and their impact on the coupling between the glacier flow and the bedrock brittle failure. Our results suggest that clustered and repeated seismic events may be correlated with transient episodes of mass ice discharge (observed by satellite GRACE and GRACE-FO experiments) through the subglacial hydrographic system that originates upstream of the glacier and extends to the grounding zone, lubricating the interface with the bedrock.

## **1 Introduction**

In the recent decades, it has become possible to deploy active and passive seismic instrumentation in the remote regions of Antarctic and Greenland. Since then, it has been demonstrated that seismic activity in polar glacial environments is controlled not so much by tectonic forces but rather by strain and stress fields due to the dynamics of the ice sheet, ice caps and large outlet glaciers (Podolskiy and Walter, 2016 and references therein). When huge masses of ice are in motion, the glacier dynamics strongly affect or even control the seismicity within the ice layer and also at the interface with the bedrock (Podolskiy and Walter, 2016) involving a broad range of frequencies of excitation of seismic waves.

It has been observed that episodes of crevassing and ice cracking (Walter et al., 2009; Colgan et al., 2016; Hudson et al. 2020), stick-slip and basal motion (Anandakrishnan and Alley, 1994; Danesi et al., 2007; Creyts et al., 2009; Smith et al., 2015; Rösli et al., 2016), iceberg calving (O’Neel et al. 2010; Bartholomaeus et al., 2012; Walter et al. 2013), glacier noise and tremor (Rösli et al., 2014), hydraulic fractures (Hudson et al. 2020), transient subglacial drainage (Winberry et al., 2009), tidal forcing (Zoet et al., 2012), are some of the main processes capable of raising the tensile and shear stress values until the exceeding of thresholds that trigger seismicity. A wide range of frequencies can be excited in the rupture processes, from icequake episodes (with characteristic frequencies of  $10^1$ - $10^2$  Hz) to tidal modulation (with characteristic frequencies of  $10^{-3}$  Hz).

The David Glacier is the largest ice stream of the Northern Victoria Land region, collecting a catchment basin of  $\sim 4\%$  of the East Antarctic Ice Sheet (Rignot, 2002) from Dome C and Talos Dome, and feeding the  $\sim 100$  km long Drygalski Ice Tongue that floats into the Ross Sea. When the glacier crosses the Transantarctic Mountains, its basal topography has a steep



38 slope change which generates an imposing icefall (~400 m downhill) and terminates in the so-called David Cauldron, at the  
39 grounding line level (Bindschadler et al., 2011).

40 For the David Glacier area, the ice speed derived from satellite radar interferometry (MEaSURES collection, Rignot et al.,  
41 2017) varies in a range between a few tens of m/y and ~700 m/y from the plateau towards the proximity of the grounding  
42 line, respectively, with strong acceleration in correspondence of the steepest topographic slopes. For its dimensions, its mas-  
43 sive ice flow, its impact on the dynamics of the front polynya, the David Glacier has been studied at length since the early  
44 90s (Frezzotti, 1993) with important outcomes concerning pioneer and revised estimates of local mass balance (Frezzotti,  
45 1997; Rignot et al., 2019), the ice thickness, surface speed and flux (Frezzotti et al., 2000; Wuite et al., 2009; Le Brocq et al.,  
46 2013; Rignot et al., 2017; Moon et al., 2021), the morphology of the bottom (Tabacco et al., 2000), the grounding line defini-  
47 tion (Bindschadler et al., 2011; Stutz et al., 2021) the subglacial lake system (Smith et al. 2009, Lindzey et al., 2019), the sta-  
48 bility of the Drygalski Ice Tongue (Indrigo et al., 2021), the glacier thinning and retreat in recent geological eras (Stutz et al.,  
49 2021).

50 Based on the analyses of NASA's Ice, Cloud and land Elevation Satellite (ICESat) laser altimeter data, Smith et al. (2009)  
51 identified the presence of six subglacial, hydrologically linked, lakes in the region of the David Glacier catchment. In accord  
52 with Pattyn (2008), the lakes would be responsible for detectable ice mass variations due to transient episodes of drainage  
53 and refilling through the subglacial hydrographic network. More recently, Indrigo et al. (2021) have demonstrated the hydro-  
54 logical continuity between the floating ice channelisation below the David Cauldron and the upstream drainage subglacial  
55 network, which would extend for about 400 km within the David Glacier drainage basin (Le Brocq et al., 2013). A similar  
56 speculation was inferred by Moon et al. (2021), who measured the David Glacier velocity changes between 2016 and 2020  
57 with the application of the offset tracking technique to Sentinel-1A SAR images. These Authors suggest that fluctuations and  
58 transient increases in the ice stream flow speed can be attributed to the injection of ice bottom water through a diffuse sub-  
59 glacial hydrological system.

60 Temporary seismological experiments have evidenced the occurrence of low-energy seismicity in the glacier area (Bannister  
61 and Kennet, 2002; Danesi et al., 2007; Zoet et al., 2012) providing interesting inferences about possible trigger mechanisms.  
62 Bannister and Kennett (2002) advanced the hypothesis that a deep tectonic lineament or, alternatively, possible fractures in  
63 the ice layer were activated; using data from a dedicated local seismic network deployed around the glacier, Danesi et al.  
64 (2007) suggested that the coupling processes between the ice flow and the bedrock activated the repeating brittle failure of  
65 one or more asperities at the ice/bedrock interface with a stick-slip mechanism; observing a significant correlation with data  
66 collected by the remote TAMSEIS (TransAntarctic Mountains Seismic Experiment) network, Zoet et al. (2012) indicated the  
67 modulation of the ocean tide as a likely forcing on repeating seismicity.

68 It is worth noting that seismological analyses in extreme scenarios such as Antarctica cannot overlook the particular environ-  
69 mental conditions. For example, by studying the occurrence of icequakes recorded near the Princess Elisabeth Antarctica  
70 Station, Frankinet et al. (2021) demonstrated that the detection threshold of seismic events in Antarctica can be influenced by  
71 weather conditions. In particular, the presence of katabatic winds can significantly increase the level of seismic noise, reduc-  
72 ing the ability to detect events.

73 In this work, we analyze the evolution of the seismicity observed in the area of David Glacier during three measurement  
74 campaigns in a 14-year long period, between November 2003 and February 2016. We observe that the seismicity shows  
75 highly clustered spatial distributions and indicates evidence of a repeated source which, on the other hand, does not reveal  
76 characteristics of continuity or seasonality over the long time that could be unequivocally correlated with regular recurrent  
77 forcing (temperature cycles, oceanic tides). Our results suggest that clustered and repeated seismic events may be correlated



with transient episodes of mass ice discharge (also observed by the Gravity Recovery and Climate Experiment GRACE and its Follow On GRACE-FO) through the subglacial hydrographic system that originates upstream of the glacier and extends to the grounding zone, lubricating the interface with the bedrock.

## 2 Methodology

### 2.1 Seismic data collection

We have collected all available seismic data registered in the study area during three Italian temporary experiments which were run along 2003/04, 2005/06 and 2015/16 austral summer campaigns around the David Glacier. During the first experiment — dated November 2003 - February 2004 and jointly conducted by an Italian/New Zealand team (Danesi et al., 2007) — 9 temporary broad-band seismic stations were installed on rock outcrops around the ice stream. The Italian team repeated temporary observations in summer campaigns 2005-06 and 2015-16 by reoccupying only the sites with the best signal-to-noise ratio (Figure 1). For these two last experiments, the seismic network was composed of 7 and 6 stations respectively.

New Zealand data and metadata are available through IRIS Data Management Center with the ZL network code (stations equipped with a CMG-40 seismic sensor and an Orion broad-band digitizer). All Italian stations (network code DY) were equipped with a Trillium T40 seismic sensor and a Reftek130-01 broad-band digitizer, powered by photovoltaic systems.

One of the Italian stations was located at Starr Nunatak (DY.STAR) in November 2003, more than 50 km away from the glacier, and during the years it has been equipped to become a semi-permanent seismic station able to record for more than 9 months per year continuously. Due to its stability and performances, the station STAR has been operating up to now providing a quasi-continuous database of daily waveforms from 2003 to 2017 (last update of the database) including data for most of the winter seasons.

All the data recovered from the experiments were organized in a SeisComp3 structure (Weber et al., 2007), which allowed us to perform a systematic and coherent analysis for the whole database.

The availability and data volume for each seismic station involved in one or more experiments between 2003 and 2016, marked by network code, is shown in the right panel of Figure 1 where it is possible to appreciate the number of stations that recorded simultaneously during each campaign.

### 2.2 New 3D seismic velocity model of the glacier based on Radio Echo Sounding data

To build a more accurate 3D glacier structural model we used all the Radio Echo Sounding (RES) datasets recorded during the campaigns conducted by the Italian National Program for Research in Antarctica (PNRA, Programma Nazionale di Ricerca in Antartide). Datasets covering a period spanning from 1995 to 2016 (<http://labetl2.rm.ingv.it/>) and the last RES measurement campaign (austral summer 2015/2016), were focused on the David Glacier area (black lines in Figure 2A) using a low-frequency version of the INGV “GlacioRadar” instrumentation operating at 12 Mhz. This particular configuration was used to integrate the lower number of bedrock reflections available in the Cauldron area in datasets collected at 60 MHz and 150 MHz (Figure 2B).

Reflection travel times were converted into depth using a constant electromagnetic (EM) wave velocity of  $168 \text{ m} \cdot \mu\text{s}^{-1}$  while cross-point analysis showed a difference in ice thickness of less than 20m in 86% of cases.



113 The 3D bedrock model of the David Glacier has been obtained by subtracting the ice thickness values from the correspond-  
114 ing RAMPDEM2 (Liu et al., 2015) elevation points for all available RES reflection points since 1995. All the elevation data  
115 (surface and bedrock) were gridded using the “IDW” (Inverse to Distance Weighting) method.

116 Figure 3 shows the overlay between the ice surface (grey) and the bedrock topography as colour-based relief with isolines at  
117 100 m. All maps are reported in UTM58S projection (WGS84).

118 Finally, we converted the model into a regular 3D matrix for seismological analyses: we first parameterized a volume of  
119  $124 \times 100 \times 23 \text{ km}^3$  over a regular-cell grid (each cell of  $0.5 \times 0.5 \times 0.5 \text{ km}^3$ ) and then we associated ice or bedrock (or both) to  
120 each cell, as a result of the difference between surface and bedrock heights in the corresponding point of the ice thickness  
121 model. For each cell, we accordingly associated the values of P-wave and S-wave velocity.

122 For ice layers, we used the compressional-wave velocity  $V_p = 3.8 \text{ km/s}$ , and the shear-wave velocity  $V_s = 2.0 \text{ km/s}$  (Röthlis-  
123 berger, 1972). For the bedrock we used  $V_p = 6.1 \text{ km/s}$  from 0 to 9.5 km depth, 6.3 km/s from 10 to 17.5 km, 6.6 km/s from  
124 depth greater than 18 km, and  $V_p/V_s$  ratio of 1.73.

125 Where the grid exceeded the area of the RES survey and direct observations were not available, we merged mean velocity  
126 values extracted from a 1D layered velocity model (Danesi et al. 2007). Given the geographical extension of the spatial dis-  
127 tribution of nodes, the final 3D velocity structure counts 2352303 values.

## 128 2.3 Seismic Data Analysis

129 The seismic database available for the three campaigns was used to characterize the evolution of the seismicity around the  
130 David Glacier. During the three summer campaigns, a network of 9, 7 and 6 seismic stations respectively was operating; dur-  
131 ing mid-seasons and many full years, only the station STAR sited in Starr Nunatak was continuously working (Figure 1).

132 We have tried to obtain a catalog as rich as possible of earthquake locations, following a 4-step scheme: 1) absolute location  
133 using a seismic 1D velocity structure; 2) absolute location using the local 3D velocity structure; 3) relative earthquake relo-  
134 cation with a double-difference approach and definition of clusters of seismicity; 4) seismic catalog enrichment using a  
135 phase-matched filter detection algorithm.

### 136 2.3.1 Absolute location - 1D velocity model

137 For summer seasons, when the full network data were available, we performed a standard absolute earthquake location by  
138 using a simple layered 1D earth velocity structure as already proposed in Danesi et al. (2007) which counts one layer of ice  
139 (1.5 km deep) overlapping four crustal layers down to 33 km depth, and a half-space. For each station, we performed an  
140 STA/LTA trigger algorithm (1 and 30 sec) to detect each variation in amplitude exceeding the signal-to-noise ratio (SNR)  
141 equal to 3, after a bandpass filter in the range 0.4-4 Hz. We merged the list of picks for each station allowing the SeisComp3  
142 (Weber et al., 2007) software to locate the events automatically when a minimum of 5 coherent P-picks was found. Each au-  
143 tomatic location was manually revised by an operator who also revised possible failures in the automatic associations. How-  
144 ever, we decided to keep the locations obtained with at least 5 arrival times recorded at least at 3 stations and with RMS less  
145 than 0.5 s.





### 146 **2.3.2 Absolute location - 3D velocity model**

147 After the manual location, the events were then relocated following a probabilistic approach with the NonLinLoc software  
 148 (Lomax et al., 2000) using the 3D velocity model which was obtained from the glacio-radar survey as described in Section  
 149 2.2.

150 The final catalog of absolute locations included more than 350 weak events ( $M_l \leq 1.8$ ) most located along the steep slope at  
 151 the entrance of the David Cauldron, where the glacier topography indicates its maximum declivity and ice flux (Figure 4).

152 In Table S1 and Figure S1 (both in the supplementary material) all the absolute locations obtained with the 3D model and  
 153 global statistic of the results are listed and shown.

### 154 **2.3.3 Relative relocation - double-difference approach**

155 Absolute locations obtained by the NonLinLoc inversion were used as input catalog for a relative double-difference location  
 156 with the HypoDD algorithm (Waldhauser and Ellsworth, 2000; Waldhauser, 2001). We intended to apply a coherent inver-  
 157 sion scheme for all data available between 2003 and 2016. After the pre-processing, more than 1700 P arrival times and  
 158 more than 500 S arrival times for 349 linked events occurring between 2003 and 2016 were selected. We defined an inver-  
 159 sion weighting scheme with weight = 1 for P-phases and weight = 0.5 for S-phases, residual threshold = 0.5 s, maximum dis-  
 160 tance allowed between linked pairs = 1 km, and damping = 80. After relocation, median residual times result lower than 0.1 s  
 161 and median spatial errors lower than 95 m, 110 m and 195 m respectively for the three coordinates x, y, z.

162 As expected and in accord with previous works (Danesi et al. 2007; Zoet et al. 2012), the centroids of the two largest clusters  
 163 (Figure 5A; 42 and 36 events respectively) were located in the David Cauldron at the foot of the icefall. A significant num-  
 164 ber of seismic episodes, collected in 8 additional clusters for a total of 61 events, occurred on top of the icefall mainly after  
 165 2005 (Table S2 in the supplementary materials).

### 166 **2.3.4 Phase-matched filter detection analysis and catalog enrichment**

167 Once the relative earthquake location catalog was completed, we applied a phase-matched filter detection technique (Cham-  
 168 berlain et al., 2017) to retrieve further possible detections and correlated repeating signals that may have escaped the classic  
 169 STA/LTA detection search.

170 We initially considered only the recordings of the 2003-04 campaign. We selected the seismic trace of a master event for  
 171 each cluster (Figure 5B) and applied the phase-matched filter technique to find correlated signals recorded at the TRIO sta-  
 172 tion which provided continuous data for the search time interval, excellent signal-to-noise ratio and relatively short distance  
 173 from cluster centroids. We used the Python-based EQcorrscan package (Chamberlain et al., 2017) on the continuous seismic  
 174 signals to perform the multi-parallel, matched-filter detection, and we were able to detect all the P and S chunks and extract  
 175 the waveforms significantly similar (cross-correlation coefficient  $\geq 0.7$ ) to the 10 selected master events representing each  
 176 cluster; afterward, we applied the Median Absolute Deviation (MAD) method to correlate the waveforms, providing more  
 177 than 1500 cross-correlated seismic signals recorded at TRIO station for the November 2003 - February 2004 time span.

178 In the left top panel of Figure 6, we show the vertical component of raw seismic signals for 46 events occurring on Julian  
 179 day 324/2003 (November 20th, 2003), filtered in the frequency band 0.4-4 Hz. The similarity among the waveforms (cross-  
 180 correlation  $\geq 0.95$ ) and signal duration reveals a common source. On the right top panel the superimposition of 1541 cross-



181 correlated signals recorded at station TRIO between November 2003 and February 2004 is shown, filtered in the frequency  
 182 range 0.4-4 Hz where most of the observed seismic energy is contained (lower panels of Figure 6).

183 To estimate the temporal variation of these events, we replicated the analysis for the detection of repeating earthquakes using  
 184 master events recorded at station STAR and we applied the phase-matched filter technique on the continuous data available  
 185 over 14 years, extending the time interval to winters and full years when the temporary seismic network was not installed.

186 After matching the detection lists, we finally achieved a catalog of repeating events (cross-correlation coefficient between  
 187 waveforms  $\geq 0.7$ ) grouped in 10 clusters, listed in Table 1. In the bottom panel of Figure 5 we show the larger groups of re-  
 188 peating events with red circles centred on cluster centroids.

### 189 **3 Results**

190 The distribution of the seismicity in space and time suggests some preliminary considerations (Figure 5 and Table 1): the  
 191 David Cauldron hosted the events with the highest similarity threshold, and a very high number of repetitions (CI\_01 and  
 192 CI\_04, nearly 1900), but the seismic activity in this area stopped abruptly and definitively after 2004. In the same period of 3  
 193 months, a very large cluster was active on the top (CI\_03, 1188 events) and, again, it stopped after 2004.

194 Two significant clusters of seismicity were continuously active between 2003 and 2016, albeit with fewer events (CI\_06 and  
 195 CI\_10, respectively 318 and 225 events). Both were located upstream of the icefall, along the main branch of the David ice  
 196 stream.

197 The remaining clusters (CL02, CL05, CL07, CL09) have numbers of events that can be disregarded in the following.

198 Two main questions need to be addressed: why the seismicity collapsed in a few tight areas and why the rate of seismicity  
 199 decreased after 2004. To unravel these questions, in the following we first evaluated possible quantitative correlations be-  
 200 tween the seismicity and the environmental parameters, the local tide modulation (as suggested in previous works by Casula  
 201 et al. 2007 and Zoet et al., 2012) and the wind speed (Frankinet et al., 2021) as possible responsible for the increase of seis-  
 202 mic noise that could decrease the efficiency of the detection.

#### 203 **3.1 Representation of seismicity and tides**

204 We extracted measurements from the database available at the permanent tide gauge observatory operating off the coast of  
 205 Terra Nova Bay about 70 km North from Drygalski Ice Tongue, in front of the Italian base Mario Zucchelli Station which  
 206 provides the hourly sampled local wave height ([https://www.geoscience.scar.org/geodesy/perm\\_ob/tide/terranova.htm](https://www.geoscience.scar.org/geodesy/perm_ob/tide/terranova.htm)).

207 As Figure 7 shows, for a few weeks after the network installation in 2003, from Julian day 320 to 355, we observe that the  
 208 repeating seismic activity presents not only similar waveforms but also regular inter-event time spacing, which stands around  
 209  $24.8 \pm 4.7$  minutes (Figure 7 a and c) in accord with previous observations (Zoet et al., 2012) and with the application of fric-  
 210 tion laws as discussed by Zoet et al. (2020).

211 The evolution of seismicity exhibits an abrupt change after Julian day 355 when the number of events per day significantly  
 212 drops and the inter-event time doubles up to  $52 \pm 15$  min. Seismicity located at the top of the David Glacier icefall remains  
 213 sustained during the following years; conversely, further repeating occurrences have not been observed in the David Caul-  
 214 dron area after 2004, suggesting that the activation of the downstream events was triggered by a transient forcing.



215 In the following, we provide some estimates of quantitative correlations between the number of seismic occurrences and en-  
216 vironmental constraints such as tidal modulation, local wind speed and ice mass variation, which could control the activation  
217 of the repeating seismic source.

### 218 **3.2 Wavelet cross-correlation with tides**

219 The correlation between the occurrence of seismicity and the variation in tidal height was verified using the cross-wavelet  
220 transform approach which allows to verify the coherence of two signals over time and to identify any common characteristic  
221 frequencies. Specifically, the inter-event time spacings of the 2003-04 seismic clusters were compared to the tide height. The  
222 WaveletComp 1.1 software through the R package was used for this purpose (Rösch and Schmidbauer, 2018).

223 As the tide heights data have one sample per hour whereas the inter-event time spacings are irregularly distributed over time,  
224 we chose to compute the upper and lower envelope of the tide time-series, because we expected a correlation with the spring  
225 and neap tides instead of higher frequency tide components, according to Figure 7. These envelopes were used to obtain the  
226 tide heights corresponding to the epoch of each event of the seismic clusters by interpolation. Interestingly, the resulting  
227 cross-wavelet power spectrum (Figure 8) implies that the inter-event time during the 5-weeks clustered seismicity is not cor-  
228 related with the tide period. Conversely, a strong correlation between the two time series can be observed just after Julian  
229 day 355 (after December 21st), with a period of 14 days and the smallest phase difference (Figure 8). This result suggests  
230 that the tidal modulation is the most probable forcing of the seismicity after day 355/2003, possibly controlling the clusters  
231 located between the grounding and the floating lines, while the source of the clustered activity before that date should be at-  
232 tributed to a different cause, limited in time and superimposed over the tidal forcing itself.

233 Indeed, the grounding and the floating lines (Figure 5B) limit the glacier volume most affected by tidal modulation, being  
234 periodically decoupled from the bedrock and rich in water-saturated sediments (till). The periodic injection of water coil  
235 favour the reduction of the basal shear stress and the acceleration of the glacier.

### 236 **3.3 Wavelet cross-correlation with wind speed and meteorological parameters**

237 For the 2003-04 campaign, we extracted the wind speed measurements for the SofiaB weather station, located 35 km up-  
238 stream from the TRIO station (Figure 1), from the open-access database "Antarctic Meteo-Climatological Observatory at  
239 MZS and Victoria Land" (<http://www.climantartide.it>).  
240 Frankinet et al. (2021) have studied the influence of the wind on the detection of seismic events during the analysis of the  
241 seismicity recorded at the Princess Elisabeth Antarctic station. Their study shows that the wind speed decreases the sensitivi-  
242 ty of the threshold seismic detection in a non-linear way. Actually, any kind of wind could increase the seismic noise back-  
243 ground but velocity higher than 6 knots (almost 12 m/s) could raise the noise up to 42dB lowering in a drastic way the num-  
244 ber of earthquakes that can be detected. In the case under study, and especially for TRIO station, the comparison between the  
245 wind speed, the root mean squared seismic noise signal and the number of seismic detection (Figure 9a) doesn't indicate a  
246 direct and simple relationship as previously postulated. In fact, the maximum number of seismic picks individuated by the  
247 STA/LTA algorithm was registered before December 1st, when the wind speed was low (<10 ktn), the presence of wind  
248 gusts (> 25 ktn) does not seem to clearly affect seismicity in terms of number of occurrences, nor the root mean squared sig-  
249 nal in the frequency band 0.1-4 Hz, i.e. the characteristic frequency band of the upstream events (Danesi et al., 2007). The  
250 number of seismic occurrences in the second half of the 2003/2004 summer campaign is always lower compared to the num-  
251 ber of detections in the first half, whatever wind speed is registered (Figure 9a).



252 Finally, we extracted the main meteorological parameters recorded at the SofiaB weather station (atmospheric pressure, air  
253 temperature, relative humidity) for the southern summer 2003-2004 and we calculated the wavelet cross-correlation between  
254 inter-event time spacing and each meteorological parameter (Figure 9b). A non-negligible correlation can be noted between  
255 Julian days 370 and 385 (January 2004) for all weather parameters, with a characteristic period of approximately 3 days. It is  
256 reasonable that in the presence of important crevasses, i.e. along the steepest stretches, liquid water percolates to the bottom  
257 of the glacier and lubricates its interface with the bedrock. It is very likely that the area upstream of the icefall was in this  
258 condition in January 2004, when clusters Cl\_01 and Cl\_03 were particularly active (Figure 5B and Table1).

### 259 3.4 Ice mass variation from GRACE measurements

260 The Gravity Recovery And Climate Experiment (GRACE; 2002-2017) and its Follow-On mission (GRACE-FO; 2018-still  
261 working) give important information related to the Earth gravity field changes due to mass variations. The Gravity Informa-  
262 tion Service (GravIS) of the German Research Centre for Geosciences (GFZ) makes available the products derived by the  
263 satellites missions GRACE and GRACE-FO (Dahle and Murboeck, 2019). In particular, the mass changes of the Antarctic  
264 Ice Sheet are provided in terms of a time-series of gridded ice-mass changes per surface area with a spatial resolution of 50  
265 km x 50 km. The David Glacier was identified in these grids inside the AIS\_315 basin (Antarctic Ice Sheet\_315). GravIS  
266 database made available the surface mass density and boundary grids for the basin, which allowed the calculation of the cor-  
267 responding variations in glacial mass pixel by pixel, with a resolution higher than the average value which can be directly  
268 downloaded from the GravIS website. The David Glacier catchment corresponds to the 7 aligned pixels represented in red in  
269 the top panel of Figure 10.

270 A noteworthy variation of ice-mass, up to 0.4 Gt, was recorded between November and December 2003, in correspondence  
271 with the 5-weeks period under investigation, when the highly correlated seismicity was active. Pixels close to the grounding  
272 line have registered an increase of mass, whereas the backward pixels are characterised by mass reduction.

273 A transient mass discharge of ice, without comparable repetitions over the following 5 years (Figure 10), was detected in the  
274 catchment area of the David Glacier, as reported by Smith et al. (2015). In particular, Smith et al. (2015) provide an estimate  
275 of the volume variation of about 1.1 km<sup>3</sup> over the 5-year between November 2003 and March 2008 possibly linked to the  
276 discharge of water from the subglacial lakes D2 and D3 and the resulting re-filling of D1 (Figure 5A), with the volume dis-  
277 placement rate rapidly soaring up in the first 6 months of the indicated period.

278 Although there are no direct observations of changes in the glacier basal conditions over the 5 weeks under study, both the  
279 GRACE measurements and the evidence provided by Smith et al. (2015) indicate that a significant circulation of water may  
280 have been injected into the subglacial drainage system below the David Glacier in that period.

281 The clustered seismic signals show variable duration between 4 and 30 sec, and frequency content concentrated in the 1-5Hz  
282 band, compatible with resonance of subglacial fluids and hydraulic transients, as illustrated by Podolskiy and Walter (2016;  
283 Figures 14 and 15 therein). Our analyses confirm that the transient injection of fluids from the top of the ice stream can be  
284 addressed as the main trigger for seismic occurrences observed at the floating zone level, between the grounding and the  
285 floating line.

## 286 4 Discussion

287 We have analysed the evolution of seismicity over a non-continuous period of 14 years around the David Glacier. We have  
288 observed two clusters of low-energy seismic events (Cl\_01 and Cl\_04 in Figure 5B and Table 1) characterised by highly cor-



289 related waveforms (cross-correlation coefficient  $\geq 0.95$ ) concentrated in a space of  $\sim 2 \text{ km}^2$  and in a time-range of 5 weeks  
290 between November and December 2003. Such repeating seismicity was recorded neither in the following months nor in the  
291 following years up to the 2015-16 austral summer campaign. Moreover, significant seismicity has occurred continuously  
292 over the 14 years (CI\_03, CI\_06, and CI\_10) along the largest ice stream that feeds the David Cauldron and channels one of  
293 the main branches of the hydrographic network. Our analyses suggest that weather conditions do not significantly affect the  
294 occurrence of seismicity,

295 It seems reasonable that the tidal modulation represents the main forcing after mid-December 2003 (Figure 8), but the origin  
296 of clusters CI\_01 and CI\_04 is more likely to be found as a transient, local, non-seasonal forcing superimposed on the tide.

297 Studies around the coupling between glaciers and the rigid and deformable beds suggest that the dominant processes by  
298 which ice advances and moves past asperities on the bedrock are regelation and plastic flow until the ice speed velocity  
299 reaches a threshold depending on environmental factors such as ice rheology and roughness (Hooke, 2005; Zoet et al., 2020)  
300 which activates the seismicity. Zoet et al. (2020) have estimated that basal stick-slip seismicity can be generally triggered  
301 when the sliding speed is between 500 and 2000 m/yr, which is compatible with the David Glacier flow velocity (Moon et al.  
302 2021 and references therein).

303 For the period 2003-04 under study, the GRACE measurements of ice mass variation show a trend compatible with the injec-  
304 tion of a sizeable amount of water into the hydrographic network beneath the David Glacier. The associated discharge would  
305 account for the increment in basal lubrication, the possible glacier acceleration, and the reduction of the basal shear stress  
306 which would favour the stick-slip seismic mechanism.

307 Recent aero-geophysical surveys of the David Glacier catchment area (Lindzey et al., 2019) suggest the revision of the sub-  
308 glacial lake locations and even cast doubts about the presence of real lakes, rather preferring the interpretation of a distrib-  
309 uted system of subglacial drainage.

310 On the other hand, significant fluctuations in the David Glacier flow velocity, characterised by sudden transient increases in  
311 the ice speed (about 5-10%) with no regularity over time, were observed by Moon et al. (2021). The Authors pointed out that  
312 the observed glacier velocities are inclined to increase during the Antarctic summer for at least three years during the 2016-  
313 2020 period probably due to the extension of the summer melt in ice surface and thus the increase of basal sliding.

314 The area of velocity increase is upstream the David Cauldron and occurs at elevation more than 600 m. AWS (Automated  
315 Weather Station) data, surface and satellite image surveys do not show any significant melting on snow surface at elevation  
316 higher than 600 m in the area of Terra Nova Bay, therefore the glacier velocity increase observed by Moon et al. 2021 should  
317 be attributed to bottom sliding rather than induced by surface melting. Unfortunately during the 2003-2004 period satellite  
318 images acquisition were not frequent enough to survey any surface velocity change.

## 319 **5 Conclusions**

320 The GRACE data relating to the austral summer 2003 reveal a mass transfer from the David Glacier catchment towards the  
321 coast which could be compatible with an emptying/filling of the regional subglacial hydrographic network and with the con-  
322 sequent acceleration of the glacier flow. The basal lubrication conditions are correlated with the seismic occurrences that we  
323 locate in correspondence with the main flows towards the Cauldron.

324 Whatever the origin or nature of the subglacial liquid water transfer, the fact remains that seismicity appears to be activated  
325 by basal lubrication, according to Zoet et al. 2020.



326 Recent measurements (Moon et al., 2021) confirm that the dynamics of the David Glacier is actually affected by transient  
327 summer pulsations of the flow velocity, in the proximity of the grounding zone, both upstream and downstream of the ice-  
328 fall, where the most numerous clusters of seismicity were located.

329 Although the seismic and satellite observations were not contemporary, we can infer that they both report a recurring (at  
330 least seasonally) behaviour in the glacier, which correlates seismic episodes with the occasional injection of liquid water into  
331 the subglacial hydraulic network.

#### 332 **Data availability**

333 All raw data can be provided by the corresponding authors upon request.

#### 334 **Author Contribution**

335 Author contribution: SD designed the experiments, carried them out, analysed the seismic data and conceived the manu-  
336 script. SS carried out the experiments and analysed seismic data. AB analysed non-seismic time series and GRACE data. SU  
337 performed the glacio-radar survey and analysed radar data. MF reviewed all available data and led the building of the con-  
338 ceptual model. SD prepared the manuscript with contributions from all co-authors.

#### 339 **Competing interests**

340 The authors declare that they have no conflict of interest.

#### 341 **Acknowledgements**

342 Maps were produced in the QGIS Geographic Information System environment, using the free database Qantarctica pro-  
343 vided by the Norwegian Polar Institute. We thank DISTART University of Bologna (IT) and DIMEC University of Modena  
344 e Reggio (IT) for providing local tide gauge data. Meteorological parameters were obtained from ‘Meteo-Climatological Ob-  
345 servatory at MZS and Victoria Land’ of PNRA - <http://www.climantartide.it>. The Gravity Information Service (GravIS, we  
346 thank Ingo Sansgen) of the German Research Centre for Geosciences (GFZ) provided observational data derived by the  
347 satellite missions.

#### 348 **Financial Support**

349 This work was supported by the Progetto Nazionale di Ricerca in Antartide (PNRA 2010/A2.09 2013/AZ2.09) funded by the  
350 Italian Ministry of Research (MUR), and by the MACMAP Project funded by Istituto Nazionale di Geofisica e Vulcanologia  
351 (Environment Department).

352



11

## 353 References

354

355 Anandakrishnan, S. and Alley, R. B.: Ice Stream C, Antarctica, sticky spots detected by microearthquake monitoring, *Ann.*  
 356 *Glaciol.*, 20, 183–186, <https://doi.org/10.1017/s0260305500016426>, 1994.

357

358 Bartholomäus, T. C., Larsen, C. F., O'Neel, S., and West, M. E., Calving seismicity from iceberg–sea surface interactions, *J.*  
 359 *Geophys. Res.*, 117, F04029, doi:10.1029/2012JF002513, 2012.

360

361 Bindshadler, R., Choi, H., Wichlacz, A., Bingham, R., Bohlander, J., Brunt, K., Corr, H., Drews, R., Fricker, H., Hall, M.,  
 362 Hindmarsh, R., Kohler, J., Padman, L., Rack, W., Rotschky, G., Urbini, S., Vornberger, P., and Young, N.: Getting around  
 363 Antarctica: new high-resolution mappings of the grounded and freely-floating boundaries of the Antarctic ice sheet created  
 364 for the International Polar Year, *Cryosphere*, 5, 569–588, doi:10.5194/tc-5-569-2011, 2011.

365

366 Casula, G., Danesi, S., Dubbini, M., and Vittuari, L.: Tidal forcing on David Glacier and Drygalski Ice Tongue in the 10 th  
 367 ISAES X Online Proceedings, 1047, 2007.

368

369 Chamberlain, C. J., Hopp, C. J., Boese, C. M., Warren-Smith, E., Chambers, D., Chu, S. X., Michailos, and K., Townend, J.:  
 370 EQcorrscan: Repeating and near-repeating earthquake detection and analysis in Python., *Seism. Res. Lett.* 89 (1): 173–181.,  
 371 doi:10.1785/0220170151, 2018.

372

373 Colgan, W., Rajaram, H., Abdalati, W., McCutchan, C., Mottram, R., Moussavi, M. S., and Grigsby, S.: Glacier crevasses:  
 374 Observations, models, and mass balance implications, *Rev Geophys*, 54, 119–161, <https://doi.org/10.1002/2015rg000504>,  
 375 2016.

376

377 Creyts, T. T., and Schoof C.G.: Drainage through subglacial water sheets, *J. Geophys. Res.*, 114, F04008,  
 378 doi:10.1029/2008JF001215, 2009.

379

380 Dahle, C., and Murboeck, M.: Post-processed GRACE/GRACE-FO Geopotential GSM Coefficients GFZ RL06 (Level-2B  
 381 Product). V. 0002. GFZ Data Services. [http://doi.org/10.5880/GFZ.GRAVIS\\_06\\_L2B](http://doi.org/10.5880/GFZ.GRAVIS_06_L2B), 2019.

382

383 Danesi, S., Bannister, S., and Morelli, A.: Repeating earthquakes from rupture of an asperity under an Antarctic outlet  
 384 glacier, *Earth Planet Sci Lett*, 253, 151–158, doi:10.1016/j.epsl.2006.10.023, 2007.

12





13

385

386 Frankinet B., Lecocq, T. and Camelbeeck, T.: Wind-induced seismic noise at the Princess Elisabeth Antarctica Station, The  
387 Cryosphere, 15, 5007–5016, doi:10.5194/tc-15-5007-2021, 2021

388

389 Frezzotti, M.: Glaciological study in Terra Nova Bay, Antarctica, inferred from remote sensing analysis. *Annals of Glaciol-*  
390 *ogy*, 17, 63–71. doi:10.3189/S0260305500012623, 1993

391

392 Frezzotti, M.: Ice front fluctuation, iceberg calving flux and mass balance of Victoria Land glaciers. *Antarctic Science*, 9(1),  
393 61–73. doi:10.1017/S0954102097000096, 1997

394

395 Frezzotti, M., Tabacco, I., & Zirizzotti, A.: Ice discharge of eastern Dome C drainage area, Antarctica, determined from air-  
396 borne radar survey and satellite image analysis. *Journal of Glaciology*, 46(153), 253–264.  
397 doi:10.3189/172756500781832855, 2000

398

399 Hooke, R.L.B.: *Principles of Glacier Mechanics* (2nd ed.). Cambridge: Cambridge University Press. doi:10.1017/  
400 CBO9780511614231, 2005

401

402 Hudson, T.S., Brisbourne, A.M., White, R.S., Kendall, J.M., Arthern, R., and Smith, A.M.: Breaking the Ice: Identifying Hy-  
403 draulically Forced Crevassing, *Geophysic. Res. Lett.*, 47, 21, <https://doi.org/10.1029/2020GL090597>, 2020.

404

405 Indrigo, C., Dow, C. F., Greenbaum, J. S., and Morlighem, M.: Drygalski Ice Tongue stability influenced by rift formation  
406 and ice morphology, *J Glaciol*, 1–10, <https://doi.org/10.1017/jog.2020.99>, 2021.

407

408 Le Brocq, A. M. L., Ross, N., Griggs, J. A., Bingham, R. G., Corr, H. F. J., Ferraccioli, F., Jenkins, A., Jordan, T. A., Payne,  
409 A. J., Rippin, D. M., and Siegert, M. J.: Evidence from ice shelves for channelized meltwater flow beneath the Antarctic Ice  
410 Sheet, *Nat Geosci*, 6, 945–948, <https://doi.org/10.1038/ngeo1977>, 2013.

411

412 Lindzey, L. E., Beem, L. H., Young, D. A., Quartini, E., Blankenship, D. D., Lee, C.-K., Lee, W. S., Lee, J. I., and Lee, J.:  
413 Aerogeophysical characterization of an active subglacial lake system in the David Glacier catchment, Antarctica, *Cryosphere*  
414 *Discuss*, 1–25, <https://doi.org/10.5194/tc-2019-217>, 2019.

415

416 Lipovsky, B. P., Meyer, C. R., Zoet, L. K., McCarthy, C., Hansen, D. D., Rempel, A. W., and Gimbert, F.: Glacier sliding,  
417 seismicity and sediment entrainment, *Ann Glaciol*, 60, 182–192, <https://doi.org/10.1017/aog.2019.24>, 2019.



15

418

419 Liu, H., K. C. Jezek, B. Li, and Z. Zhao.: Radarsat Antarctic Mapping Project Digital Elevation Model, Version 2. [Indicate  
420 subset used]. Boulder, Colorado USA. NASA National Snow and Ice Data Center Distributed Active Archive Center.  
421 doi:10.5067/8JKNEW6BFRVD., 2015. [last accessed 11/2021].

422

423 Lomax A., Virieux J., Volant P., and Berge-Thierry C.: Probabilistic Earthquake Location in 3D and Layered Models. In:  
424 Thurber C.H., Rabinowitz N. (eds) Advances in Seismic Event Location. Modern Approaches in Geophysics, vol 18.  
425 Springer, Dordrecht, doi:10.1007/978-94-015-9536-0\_5, 2000.

426

427 Moon J., Cho Y. and Hoonyol L.: Flow Velocity Change of David Glacier, East Antarctica, from 2016 to 2020 Observed by  
428 Sentinel-1A SAR Offset Tracking Method, Korean J. of Remote Sensing, 37(1),

429 1-11, <https://doi.org/10.7780/kjrs.2021.37.1.1.1>, 2021

430

431 Mouginot, J., B. Scheuchl, and E. Rignot.: Mapping of Ice Motion in Antarctica Using Synthetic-Aperture Radar Data, Re-  
432 mote Sensing. 4. 2753-2767, doi:10.3390/rs4092753, 2012

433

434 O'Neel, S., Larsen, C. F., Rupert, N., and Hansen, R.: Iceberg calving as a primary source of regional-scale glacier-generated  
435 seismicity in the St. Elias Mountains, Alaska, J. Geophys. Res., 115, F04034, doi:10.1029/2009JF001598, 2010.

436

437 Pattyn, F.: Investigating the stability of subglacial lakes with a full Stokes ice-sheet model. J. Glaciol., 54 (185), 353–361,  
438 doi: 10.3189/002214308784886171, 2008.

439

440 Podolskiy, E. A. and Walter, F.: Cryoseismology, Rev Geophys, 54, 708–758, doi:10.1002/2016rg000526, 2016.

441

442 Rignot, E.: Mass balance of East Antarctic glaciers and ice shelves from satellite data, Annals of Glaciology, 34, 217–227,  
443 2002.

444

445 Rignot, E., Mouginot J., and Scheuchl B.: Ice Flow of the Antarctic Ice Sheet, Science. 333, 1427-1430, doi:10.1126/scien-  
446 ce.1208336, 2011.

447



- 17  
448 Rignot, E., J. Mouginot, and B. Scheuchl., MEaSUREs InSAR-Based Antarctica Ice Velocity Map, Version 2. Boulder, Col-  
449 orado USA. NASA National Snow and Ice Data Center Distributed Active Archive Center, doi:10.5067/D7GK8F5J8M8R,  
450 2017. [last accessed 11/2021].
- 451
- 452 Rössli, C., Walter, F., Husen, S., Andrews, L., Lüthi, M., Catania, G., and Kissling, E.: Sustained seismic tremors and ice-  
453 quakes detected in the ablation zone of the Greenland ice sheet. *Journal of Glaciology*, 60 (221) , 563-575.  
454 doi:10.3189/2014JG13J210, 2014.
- 455
- 456 Rössli, C., Helmstetter, A., Walter, F., and Kissling, E.: Meltwater influences on deep stick-slip icequakes near the base of  
457 the Greenland Ice Sheet, *J Geophys Res Earth Surf*, 121, 223–240, <https://doi.org/10.1002/2015jf003601>, 2016.
- 458
- 459 Röthlisberger, H. Seismic exploration in cold regions, Tech. Rep., Cold Regions Research and Engineering Laboratory,  
460 Hanover, N. H. Roux, P.-F., D. Marsan, J.-P. Métaixian, G. O'Brien, and L. Moreau (2008), Microseismic activity within a  
461 serac zone in an Alpine glacier (Glacier d'Argentiere, Mont Blanc, France), *J. Glaciol.*, 54(184), 157–168,  
462 doi:10.3189/002214308784409053, 1972.
- 463
- 464 Rösch, A. and Schmidbauer, H.: WaveletComp 1.1: A guided tour through the R package, 2018.
- 465
- 466 RStudio Team: RStudio: Integrated Development for R. RStudio, PBC, Boston, MA URL <http://www.rstudio.com/>, 2020.
- 467
- 468 Smith, B., Fricker, H.A., Joughin, I., and Tulaczyk, S.: An inventory of active subglacial lakes in Antarctica detected by  
469 ICESat (2003–2008), *Journal of Glaciology*, 55(192), 573-595, doi:10.3189/002214309789470879, 2009.
- 470
- 471 Smith, E. C., Smith, A. M., White, R. S., Brisbourne, A. M., and Pritchard, H. D.: Mapping the ice-bed interface characteris-  
472 tics of Rutford Ice Stream, West Antarctica, using microseismicity, *J Geophys Res Earth Surf*, 120, 1881–1894, [https://](https://doi.org/10.1002/2015jf003587)  
473 doi.org/10.1002/2015jf003587, 2015.
- 474
- 475 Stutz, J., Mackintosh, A., Norton, K., Whitmore, R., Baroni, C., Jamieson, S. S. R., Jones, R. S., Balco, G., Salvatore, M. C.,  
476 Casale, S., Lee, J. I., Seong, Y. B., McKay, R., Vargo, L. J., Lowry, D., Spector, P., Christl, M., Ochs, S. I., Nicola, L. D.,  
477 Iarossi, M., Stuart, F., and Woodruff, T.: Mid-Holocene thinning of David Glacier, Antarctica: chronology and controls,  
478 *Cryosphere*, 15, 5447–5471, <https://doi.org/10.5194/tc-15-5447-2021>, 2021.
- 479



- 19  
480 Tabacco, I., Bianchi, C., Chiappini, M., Zirizzotti, A., and Zuccheretti, E.: Analysis of bottom morphology of the David Gla-  
481 cier–Drygalski Ice Tongue, East Antarctica. *Annals of Glaciology*, 30, 47–51. doi:10.3189/172756400781820624, 2000
- 482
- 483 Waldhauser, F. and Ellsworth, W.: A Double-Difference Earthquake Location Algorithm: Method and Application to the  
484 Northern Hayward Fault, California, *Bulletin of the Seismological Society of America*, 90, 1353–1368,  
485 doi:10.1785/0120000006, 2000.
- 486
- 487 Waldhauser, F.: hypoDD—A Program to Compute Double-Difference Hypocenter Locations: U.S. Geological Survey Open-  
488 File Report 01-113, 25 pp., <https://pubs.usgs.gov/of/2001/0113/>, 2001.
- 489
- 490 Walter, F., Clinton, J. F., Deichmann, N., Dreger, D. S., Minson, S. E., and Funk, M.: Moment Tensor Inversions of  
491 Icequakes on Gornergletscher, SwitzerlandMoment Tensor Inversions of Icequakes on Gornergletscher, Switzerland, *B*  
492 *Seismol Soc Am*, 99, 852–870, <https://doi.org/10.1785/0120080110>, 2009.
- 493
- 494 Walter, F., Olivieri, M., and Clinton, J. F.: Calving event detection by observation of seiche effects on the Greenland fjords,  
495 *J Glaciol*, 59, 162–178, <https://doi.org/10.3189/2013jog12j118>, 2013.
- 496
- 497 Winberry, J. P., Anandakrishnan, S., and Alley, R. B.: Seismic observations of transient subglacial water-flow beneath  
498 MacAyeal Ice Stream, West Antarctica, *Geophys. Res. Lett.*, 36, L11502, doi:10.1029/2009GL037730, 2009.
- 499
- 500 Wuite, J., Jezek, K. C., Wu, X., Farness, K., and Carande, R.: The velocity field and flow regime of David Glacier and Dry-  
501 galski Ice Tongue, Antarctica, *Polar Geogr*, 32, 111–127, <https://doi.org/10.1080/10889370902815499>, 2009.
- 502
- 503 Zoet, L., Anandakrishnan, S., Alley, R., Nyblade, A., and Wiens, D.: Motion of an Antarctic glacier by repeated tidally mod-  
504 ulated earthquakes. *Nature Geoscience*, 5, 623–626, doi:10.1038/ngeo1555, 2012.
- 505
- 506 Zoet, L. K., Ikari, M. J., Alley, R. B., Marone, C., Anandakrishnan, S., Carpenter, B. M., and Scuderi, M. M.: Application of  
507 Constitutive Friction Laws to Glacier Seismicity, *Geophys Res Lett*, 47, <https://doi.org/10.1029/2020gl088964>, 2020.



21

## 508 Figure Caption

509

510 **Figure 1:** On the left, map of the seismic networks in operation between 2003 and 2016 around the David Glacier. Circles  
 511 and crosses are used for seismic station sites, coloured in agreement with legend. The meteorological station SofiaB and the  
 512 tide gauge (installed at Mario Zucchelli Station) are plotted with green triangles. The DEM is extracted from RAMP2 Eleva-  
 513 tion Model (200m; Liu et al. 2015). The plot on the right shows the availability of the waveforms included in the database.  
 514 DY: Italian network, ZL: New Zealand network. STAR is a semi-permanent Italian seismic station which has been working  
 515 up to now since 2003.

516

517 **Figure 2:** PNRA RES data coverage in the David Glacier area: A) Flight tracks; B) Radargram at 12 MHz frequency obtained  
 518 in the Cauldron area.

519

520 **Figure 3:** David Glacier area - 3D model of RAMPDEM topographic surface (gray) overlaid to the bedrock elevation (color  
 521 scaled; isolines at 100m) derived by PNRA RES datasets (Vertical exaggeration=16).

522

523 **Figure 4:** Map of epicentres obtained with the standard absolute location of events occurring during austral summers 2003-  
 524 04, 2005-06, 2015-16 when all seismic stations were recording.

525

526 **Figure 5:** A) Distribution of seismicity located in this work and its evolution in space and time: 2003-04 austral summer (red  
 527 crosses), 2005-06 austral summer (orange crosses), 2015-16 austral summer (blue crosses). The map is developed in a QGIS  
 528 environment, the DEM is extracted from RAMP2 Elevation Model (200m; Liu et al. 2015); the ice flow speed vector field is  
 529 extracted from MEASUREs (Rignot et al. 2011, Rignot et al. 2017; Mouginot et al. 2011); subglacial lakes are extracted from  
 530 the compilation of Smith et al. (2009) - named according to the same nomenclature; the subglacial water flux is from Le-  
 531 Brocq et al., 2013; the grounding (blue) and hydrostatic (green) lines are extracted from ASAD (Bindshadler et al., 2011).  
 532 The red square marks the area enlarged in panel B.  
 533 B) a detailed view of the repeating earthquakes: the red circles indicate clusters and the numbered labels indicate the cumula-  
 534 tive occurrences for each cluster over 14 years (when larger than 50). Topography and glaciological information as in the  
 535 general map.

536

537 **Figure 6:** Top left) 46 vertical components of raw seismic signals recorded at station TRIO on Julian day 324/2003, filtered  
 538 in the frequency band 0.4 - 4 Hz. Signals have cross-correlation coefficients greater than 0.95. Top right) superimposition of  
 539 the vertical components of 1541 correlated events, recorded at station TRIO between November 2003 and January 2004.  
 540 Bottom panel) Frequency contents of the corresponding events for TRIO station.

541



23

542 **Figure 7:** a) Horizontal axis is time, expressed in days after 01/01/2003. In blue local ocean wave height as measured by tide  
 543 gauge (primary vertical axis), in red inter-event time spacing between consecutive events in minutes (secondary vertical  
 544 axis). b) In blue the local ocean wave height, as in the top panel, the green line shows the number of seismic events per day  
 545 (secondary vertical axis). c) and d) the histograms show the distribution of inter-event time spacings for a reduced set and the  
 546 full set, respectively. The corresponding Probability Density Functions (PDF) are superimposed, the vertical dark green lines  
 547 give the mode value.

548

549 **Figure 8:** Cross-wavelet power spectrum between the tide heights and the inter-event time spacing of the seismic events as a  
 550 function of time (horizontal axis is the 2003 Julian day). The coloured scale indicates the cross-wavelet power level at each  
 551 period. Black arrows indicate the phase shift between the two time-series: when arrows point to the right the time-series are  
 552 in phase, when arrows point to the left they are in counter phase. Note the logarithmic vertical scale. The white lines delineate  
 553 the statistically significant areas, at 10% significance level against a white noise null.

554

555 **Figure 9:** Panel A) Hourly wind speed recovered from meteorological station SofiaB during the 3 months November 2003-  
 556 February 2004 (central panel). The comparison between daily noise (upper) in the two main frequencies of seismic events  
 557 (0.1-4 Hz) and wind (5-15 Hz) and the number of picks obtained by the STA/LTA detection of station TRIO (lower panel)  
 558 seems to exclude any correlation with the wind speed.  
 559 Panel B) Cross-wavelet power spectrum between meteorological parameters and the inter-event time spacing of the seismic  
 560 occurrences. Coloured scales indicate the cross-wavelet power level at each period - note different scales for each plot. Hori-  
 561 zontal arrows pointing to the right indicate that the two signals are in phase at the corresponding period. The white lines de-  
 562 lineate the statistically significant areas, at 10% significance level against a white noise null as in Figure 8.

563

564 **Figure 10:** Ice-mass variation in the David Glacier area observed by GRACE. Left panel: the blue line surrounds the region  
 565 AIS\_315 as in the GravIS catalog. The red area corresponds to the 7 cells (pixels) providing data for this study. Right panel:  
 566 variation in Gton of ice mass for each cell and each year between 2003 and 2016 represented in accord with the colour scale,  
 567 recorded by GRACE and GRACE-FO.

568

569

570 |

571 |

572 |

573 |

574 |

575 |

576 |

24



25

577 **Table Caption**

578 **Table 1:** Geographic coordinates of the centroids of seismic clusters and number of annual occurrences.

579

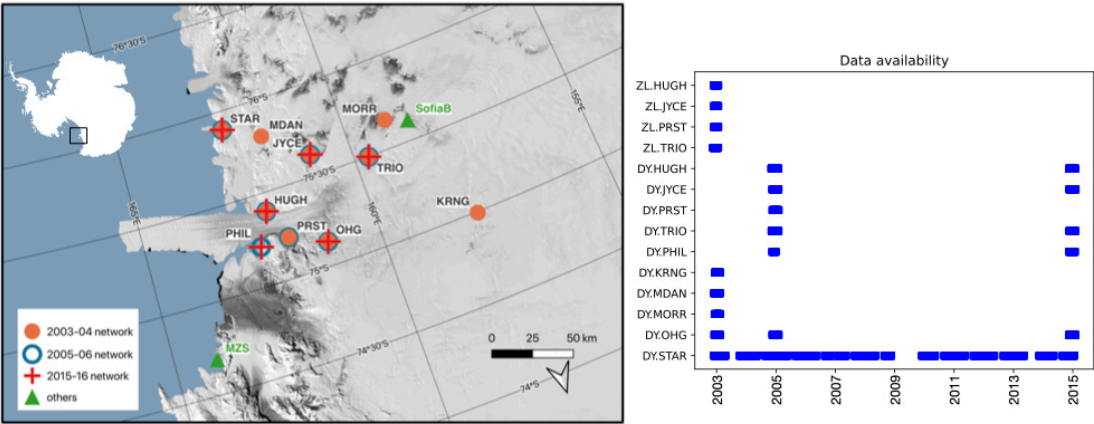
Cluster Centroid coordinates			Number of detections per year														Tot
	Lat (deg)	Long (deg)	2003	2004	2005	2006	2007	2008	2009	2010	2011	2012	2013	2014	2015	2016	
Cl_01	-75.367	160.839	803	853	2	5	3	3	0	0	1	0	0	1	2	0	1673
Cl_02	-75.330	160.405	13	0	0	0	0	0	0	0	0	0	0	0	0	0	13
Cl_03	-75.385	160.511	678	510	0	0	0	0	0	0	0	0	0	0	0	0	1188
Cl_04	-75.367	160.850	97	93	0	0	0	0	0	0	0	0	0	0	0	0	190
Cl_05	-75.306	160.333	0	0	1	0	0	0	0	0	0	0	0	0	0	0	1
Cl_06	-75.331	160.399	2	6	16	21	20	25	18	1	21	30	27	14	24	0	225
Cl_07	-75.289	160.836	1	0	0	0	1	0	0		0	1	2	1	1	1	8
Cl_08	-75.236	160.693	0	0	1	0	0	0	0	0	0	0	0	0	0	0	1
Cl_09	-75.292	160.760	1	3	7	11	9	2	3	0	3	3	2	5	3	1	53
Cl_10	-75.387	160.434	0	3	14	186	22	17	14	3	18	7	10	15	9	0	318
		Tot	1595	1468	41	223	55	47	35	4	43	41	41	36	39	2	

580



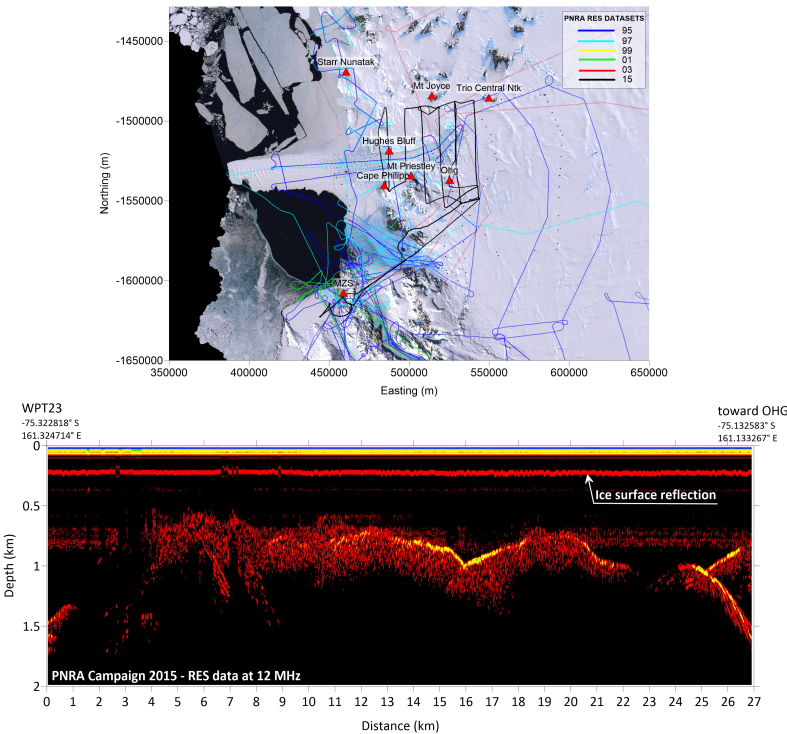


FIGURE 1



**Figure 1:** On the left, map of the seismic networks in operation between 2003 and 2016 around the David Glacier. Circles and crosses are used for seismic station sites, coloured in agreement with legend. The meteorological station SofiaB and the tide gauge (installed at Mario Zucchelli Station) are plotted with green triangles. The DEM is extracted from RAMP2 Elevation Model (200m; Liu et al. 2015). The plot on the right shows the availability of the waveforms included in the database. DY: Italian network, ZL: New Zealand network. STAR is a semi-permanent Italian seismic station which has been working up to now since 2003.

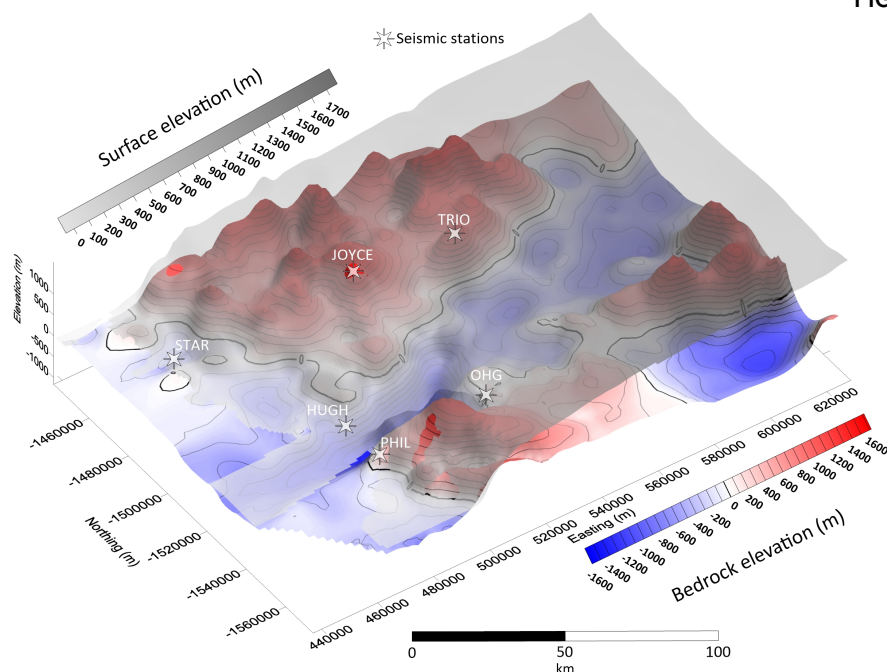
FIGURE 2



**Figure 2:** PNRA RES data coverage in the David Glacier area: A) Flight tracks; B) Radargram at 12 MHz frequency obtained in the Cauldron area.

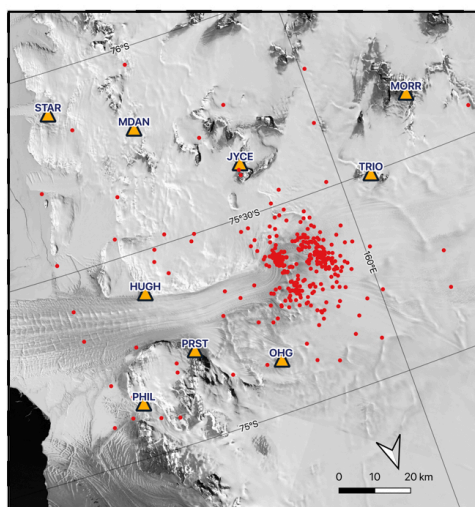


FIGURE 3



**Figure 3:** David Glacier area - 3D model of RAMPDEM topographic surface (gray) overlaid to the bedrock elevation (color scaled; isolines at 100m) derived by PNRA RES datasets (Vertical exaggeration=16).

FIGURE 4



**Figure 4:** Map of epicentres obtained with the standard absolute location of events occurring during austral summers 2003-04, 2005-06, 2015-16 when all seismic stations were recording.



Figure 5

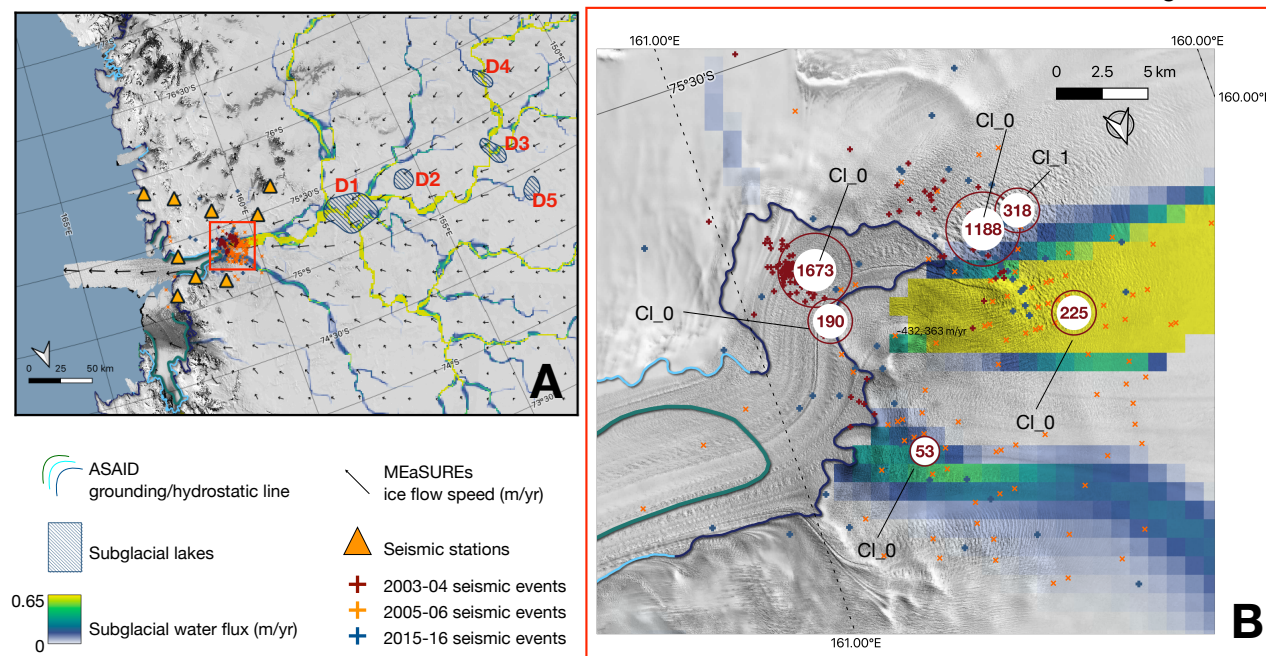


**Figure 5:** A) Distribution of seismicity located in this work and its evolution in space and time: 2003-04 austral summer (red crosses), 2005-06 austral summer (orange crosses), 2015-16 austral summer (blue crosses). The map is developed in a QGIS environment, the DEM is extracted from RAMP2 Elevation Model (200m; Liu et al. 2015); the ice flow speed vector field is extracted from MEaSUREs (Rignot et al. 2011, Rignot et al. 2017; Mougnot et al. 2011); subglacial lakes are extracted from the compilation of Smith et al. (2009) - named according to the same nomenclature; the subglacial water flux is from LeBrocq et al., 2013; the grounding (blue) and hydrostatic (green) lines are extracted from ASAID (Bindshadler et al., 2011). The red square marks the area enlarged in panel B.

B) a detailed view of the repeating earthquakes: the red circles indicate clusters and the numbered labels indicate the cumulative occurrences for each cluster over 14 years (when larger than 50). Topography and glaciological information as in the general map.

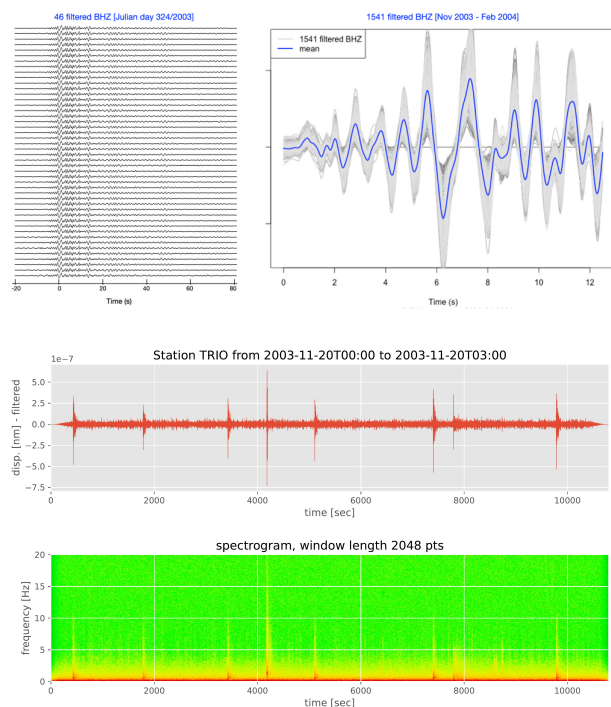


Figure 6

**Figure 6:** Top left) 46 vertical components of raw seismic signals recorded at station TRIO on Julian day 324/2003, filtered in the frequency band 0.4 - 4 Hz. Signals have cross-correlation coefficients greater than 0.95. Top right) superimposition of the vertical components of 1541 correlated events, recorded at station TRIO between November 2003 and January 2004. Bottom panel) Frequency contents of the corresponding events for TRIO station.

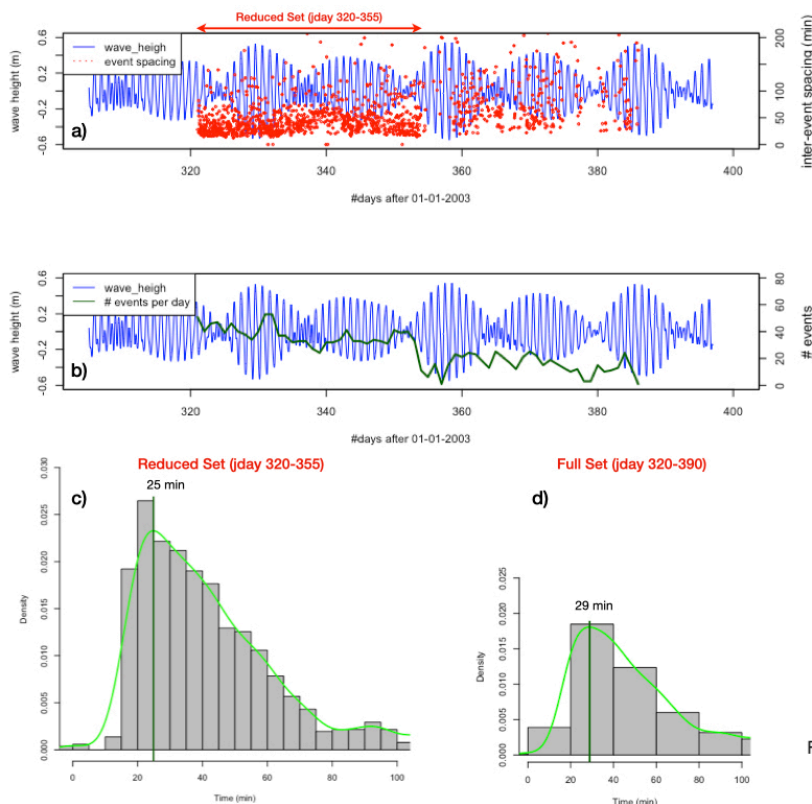


FIGURE 7

**Figure 7:** a) Horizontal axis is time, expressed in days after 01/01/2003. In blue local ocean wave height as measured by tide gauge (primary vertical axis), in red inter-event time spacing between consecutive events in minutes (secondary vertical axis). b) In blue the local ocean wave height, as in the top panel, the green line shows the number of seismic events per day (secondary vertical axis). c) and d) the histograms show the distribution of inter-event time spacings for a reduced set and the full set, respectively. The corresponding Probability Density Functions (PDF) are superimposed, the vertical dark green lines give the mode value.

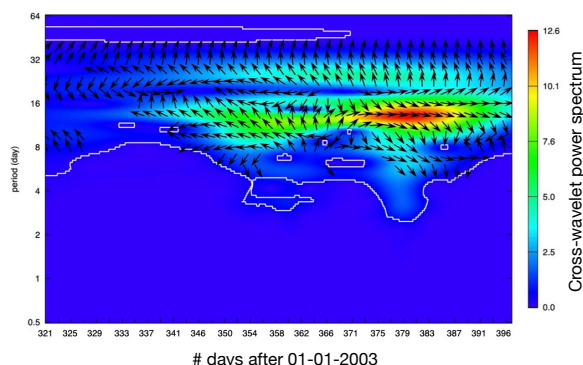


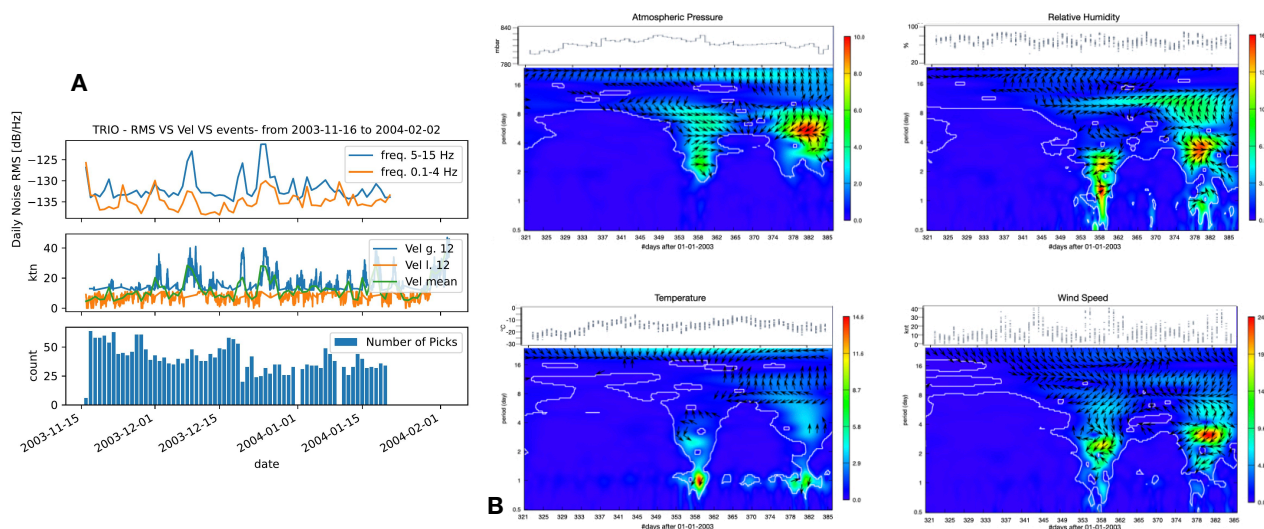
FIGURE 8

**Figure 8:** Cross-wavelet power spectrum between the tide heights and the inter-event time spacing of the seismic events as a function of time (horizontal axis is the 2003 Julian day). The coloured scale indicates the cross-wavelet power level at each period. Black arrows indicate the phase shift between the two time-series: when arrows point to the right the time-series are in phase, when arrows point to the left they are in counter phase. Note the logarithmic vertical scale. The white lines delineate the statistically significant areas, at 10% significance level against a white noise null.



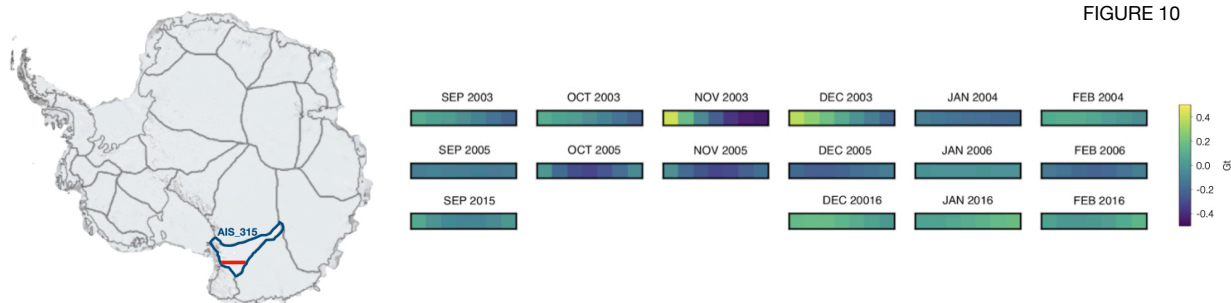


FIGURE 9



**Figure 9:** Panel A) Hourly wind speed recovered from meteorological station SofiaB during the 3 months November 2003-February 2004 (central panel). The comparison between daily noise (upper) in the two main frequencies of seismic events (0.1-4 Hz) and wind (5-15 Hz) and the number of picks obtained by the STA/LTA detection of station TRIO (lower panel) seems to exclude any correlation with the wind speed. Panel B) Cross-wavelet power spectrum between meteorological parameters and the inter-event time spacing of the seismic occurrences. Coloured scales indicate the cross-wavelet power level at each period - note different scales for each plot. Horizontal arrows pointing to the right indicate that the two signals are in phase at the corresponding period. The white lines delineate the statistically significant areas, at 10% significance level against a white noise null as in Figure8.

FIGURE 10



**Figure 10:** Ice-mass variation in the David Glacier area observed by GRACE. Left panel: the blue line surrounds the region AIS\_315 as in the GravIS catalog. The red area corresponds to the 7 cells (pixels) providing data for this study. Right panel: variation in Gton of ice mass for each cell and each year between 2003 and 2016 represented in accord with the colour scale, recorded by GRACE and GRACE-FO.